



## OPEN ACCESS

EDITED BY  
Huayang Zhang,  
University of Adelaide, Australia

REVIEWED BY  
Shengwei Deng,  
Zhejiang University of Technology, China  
Yun-Xiang Pan,  
Shanghai Jiao Tong University, China

\*CORRESPONDENCE  
Xi Li,  
✉ xili21@mail.zjxu.edu.cn  
Yongyong Cao,  
✉ cyy@zjxu.edu.cn

†These authors have contributed equally to this work

SPECIALTY SECTION  
This article was submitted to Green and Sustainable Chemistry, a section of the journal *Frontiers in Chemistry*

RECEIVED 10 January 2023  
ACCEPTED 30 January 2023  
PUBLISHED 09 February 2023

CITATION  
An R, Chen X, Fang Q, Meng Y, Li X and Cao Y (2023), Structure–activity relationship of Cu-based catalysts for the highly efficient CO<sub>2</sub> electrochemical reduction reaction.  
*Front. Chem.* 11:1141453.  
doi: 10.3389/fchem.2023.1141453

COPYRIGHT  
© 2023 An, Chen, Fang, Meng, Li and Cao. This is an open-access article distributed under the terms of the [Creative Commons Attribution License \(CC BY\)](https://creativecommons.org/licenses/by/4.0/). The use, distribution or reproduction in other forums is permitted, provided the original author(s) and the copyright owner(s) are credited and that the original publication in this journal is cited, in accordance with accepted academic practice. No use, distribution or reproduction is permitted which does not comply with these terms.

# Structure–activity relationship of Cu-based catalysts for the highly efficient CO<sub>2</sub> electrochemical reduction reaction

Runzhi An<sup>1†</sup>, Xuanqi Chen<sup>1†</sup>, Qi Fang<sup>1</sup>, Yuxiao Meng<sup>1,2</sup>, Xi Li<sup>1\*</sup> and Yongyong Cao<sup>1\*</sup>

<sup>1</sup>College of Biological, Chemical Science and Engineering, Jiaying University, Jiaying, Zhejiang, China, <sup>2</sup>College of Chemical Engineering, State Key Laboratory Breeding Base of Green-Chemical Synthesis Technology, Zhejiang University of Technology, Hangzhou, China

Electrocatalytic carbon dioxide reduction (CO<sub>2</sub>RR) is a relatively feasible method to reduce the atmospheric concentration of CO<sub>2</sub>. Although a series of metal-based catalysts have gained interest for CO<sub>2</sub>RR, understanding the structure–activity relationship for Cu-based catalysts remains a great challenge. Herein, three Cu-based catalysts with different sizes and compositions (Cu@CNTs, Cu<sub>4</sub>@CNTs, and CuNi<sub>3</sub>@CNTs) were designed to explore this relationship by density functional theory (DFT). The calculation results show a higher degree of CO<sub>2</sub> molecule activation on CuNi<sub>3</sub>@CNTs compared to that on Cu@CNTs and Cu<sub>4</sub>@CNTs. The methane (CH<sub>4</sub>) molecule is produced on both Cu@CNTs and CuNi<sub>3</sub>@CNTs, while carbon monoxide (CO) is synthesized on Cu<sub>4</sub>@CNTs. The Cu@CNTs showed higher activity for CH<sub>4</sub> production with a low overpotential value of 0.36 V compared to CuNi<sub>3</sub>@CNTs (0.60 V), with \*CHO formation considered the potential-determining step (PDS). The overpotential value was only 0.02 V for \*CO formation on the Cu<sub>4</sub>@CNTs, and \*COOH formation was the PDS. The limiting potential difference analysis with the hydrogen evolution reaction (HER) indicated that the Cu@CNTs exhibited the highest selectivity of CH<sub>4</sub> among the three catalysts. Therefore, the sizes and compositions of Cu-based catalysts greatly influence CO<sub>2</sub>RR activity and selectivity. This study provides an innovative insight into the theoretical explanation of the origin of the size and composition effects to inform the design of highly efficient electrocatalysts.

## KEYWORDS

electrochemical CO<sub>2</sub> reduction reaction (CO<sub>2</sub>RR), Cu-based catalysts, density functional theory (DFT), size effect, compositional effect

## 1 Introduction

With the rapid development of the global society, the increasing emissions of carbon dioxide (CO<sub>2</sub>) from the burning of fossil fuels have led to serious environmental and energy crises (Jiao, 2019; Cao et al., 2021; Wang et al., 2022). The electrocatalytic CO<sub>2</sub> reduction reaction (CO<sub>2</sub>RR) provides a viable alternative to convert CO<sub>2</sub> into value-added chemical products such as carbon monoxide (CO), methane (CH<sub>4</sub>), methanol (CH<sub>3</sub>OH), ethylene (CH<sub>2</sub>CH<sub>2</sub>), and ethanol (CH<sub>3</sub>CH<sub>2</sub>OH) (Xue et al., 2020; Zhang, 2022; Zhou et al., 2022). Therefore, this is a promising approach to alleviate the global demand for fossil fuels and greenhouse effects. In addition, the advantages of CO<sub>2</sub>RR include 1) the feasibility of controlling the process by adjusting the potential and related conditions; 2) electricity consumption from sustainable sources such as the Sun and wind; 3) electrochemical reaction systems that are compact, modular, and easily scaled-up (Gong et al., 2019; Jiao et al., 2019; Bai et al., 2020; Han

et al., 2020; He et al., 2020). However, there remain several challenges to the practical application of CO<sub>2</sub>RR, such as slow reaction kinetics, poor efficiency, and low product selectivity due to the strong C=O double bond (806 kJ.mol<sup>-1</sup>) in CO<sub>2</sub> molecules (Alvarez et al., 2017). Therefore, highly active electrocatalysts must be designed to improve the sluggish kinetics and energy conversion efficiency.

A recent study demonstrated the high activity and selectivity of transition metal catalysts in the conversion of CO<sub>2</sub> to CO, CH<sub>4</sub>, or CH<sub>3</sub>OH. Among these, Cu-based catalysts have been widely applied to CO<sub>2</sub>RR due to their excellent conductivity and availability (Li et al., 2017). The catalyst size and composition structure are usually regulated to tune the catalytic activity and selectivity of metal nanoparticles. Varying particle size has size effects in CO<sub>2</sub>RR. Studies have reported on the CO<sub>2</sub>RR trends over spherical Cu nanoparticles ranging in size from 2 to 15 nm (Shen et al., 2021). A decrease in Cu nanoparticle size leads to a significant increase in low coordination sites, resulting in strong CO<sub>2</sub> adsorption and hydrogenation. A series of different sizes of Ni-based catalysts (Ni@CNT, Ni<sub>4</sub>@CNT, and Ni (110)) were also designed to study their size effects in CO<sub>2</sub>RR. Density functional theory (DFT) calculations revealed that the Ni@CNT catalyst is much more conducive to the conversion of CO<sub>2</sub> to CO, while CH<sub>4</sub> molecules were produced on Ni@CNT and Ni (100) with increasing Ni size (Cao et al., 2020a). Therefore, the catalyst size may affect CO<sub>2</sub> activation and final products.

The alloy effect of the metal catalyst is another key factor in catalytic reactions. The electronic structure of metal catalysts can be controlled by alloying with other metal atoms, which is an obvious characteristic of Cu-based catalysts (Weng et al., 2018; Meng et al., 2022). A Cu–Ni alloy catalyst embedded in the N-doped carbon framework (CuNi/NC) synthesized for CO<sub>2</sub>RR showed excellent activity and selectivity for electrocatalytic CO<sub>2</sub>RR to CO, with a high Faradaic efficiency of 99.7% and a potential of –0.6 V (Zhang, 2019; Zhong et al., 2020). Additionally, a non-noble metal CuSn alloy with a different Cu–Sn composition demonstrated a completely different distribution of products for CO<sub>2</sub>RR, including CO and formate (Li et al., 2020a). Tuning the surface composition of Cu-based catalysts *via* alloying with other metals could directly modify the adsorbed state of the intermediate species on their active sites and determine the final product during the CO<sub>2</sub>RR. Therefore, the introduction of other metals is an effective strategy to adjust the electronic structure and improve CO<sub>2</sub>RR activity and selectivity.

This study designed different sizes and compositions of Cu-based catalysts (Cu@CNT, Cu<sub>4</sub>@CNT, and CuNi<sub>3</sub>@CNT) to explore the relationship between the structure of catalysts and activity for CO<sub>2</sub>RR based on DFT calculations. CO<sub>2</sub> molecule adsorption and activation are essential for the following hydrogenation steps. Therefore, different CO<sub>2</sub> adsorption configurations were optimized to explore the nature of CO<sub>2</sub> activation on the three catalysts by analyzing their geometric and electronic properties. The mechanisms of CO<sub>2</sub>RR on different Cu-based catalysts were also assessed, and a plot was constructed to compare the selectivity of CO<sub>2</sub>RR among Cu@CNT, Cu<sub>4</sub>@CNT, and CuNi<sub>3</sub>@CNT.

## 2 Computational models and methods

All calculations were performed using the Vienna *Ab initio* Simulation Package (VASP) (Kresse and Hafner, 1993; Kresse and

Furthmüller, 1996), including the Perdew–Burke–Ernzerhof (PBE) functions in the generalized gradient approximation (GGA) to describe electron exchange and correction effect (Blochl, 1994; Perdew et al., 1996; Kresse and Joubert, 1999). The cutoff energy for the plane wave basis was set to 520.0 eV. The Brillouin zone was sampled at 4 × 4 × 1 *k* points for all calculation models using the Monkhorst–Pack grid. The convergence criteria for energy for geometry optimization were set to 1.0 × 10<sup>-5</sup> eV. The vacuum thickness was 15.0 Å to prevent interlayer interactions. van der Waals correction was implemented using the Grimme's DFT-D3 method (Krieg, 2010).

The adsorption energy ( $E_{\text{ads}}$ ) of CO<sub>2</sub> is calculated using the following equation:

$$E_{\text{ads}} = E_{\text{cat+mol}} - E_{\text{cat}} - E_{\text{mol}}, \quad (1)$$

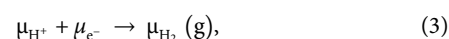
where  $E_{\text{cat+mol}}$  is the total energy of CO<sub>2</sub> molecule or intermediate adsorption on Cu@CNTs, Cu<sub>4</sub>@CNTs, and CuNi<sub>3</sub>@CNTs;  $E_{\text{cat}}$  is the optimized energy of three catalysts; and  $E_{\text{mol}}$  is the energy of the adsorbed molecule.

The binding energy ( $E_{\text{b}}$ ) of a single Cu atom, Cu<sub>4</sub>, and CuNi<sub>3</sub> cluster anchored on N-doped CNT is defined as follows:

$$E_{\text{b}} = E_{\text{total}} - E_{\text{N-CNT}} - E_{\text{metal}}, \quad (2)$$

where  $E_{\text{total}}$  is the total energy of Cu@CNTs, Cu<sub>4</sub>@CNTs, and CuNi<sub>3</sub>@CNTs;  $E_{\text{N-CNT}}$  denotes the optimized energy of N-doped CNT support; and  $E_{\text{metal}}$  is the energy of a single Cu atom or Cu<sub>4</sub> or the Cu<sub>3</sub>Ni cluster.

The computational hydrogen electrode (CHE) mode was proposed by Nørskov et al (Nadolska et al., 2021), in which the changes in Gibbs free energies of CO<sub>2</sub>RR are calculated for every elementary step. The reference electrode is the reversible hydrogen electrode (RHE). Therefore, the chemical potential ( $\mu$ ) of the proton–electron pair is defined as follows:



The change in Gibbs free energy ( $\Delta G$ ) for each elementary step is determined by the following equation:

$$\Delta G = \Delta E + \Delta E_{\text{ZPE}} - T\Delta S + \Delta G_U, \quad (4)$$

where  $\Delta E_{\text{DFT}}$  is the change of electron energy calculated by the DFT calculation,  $\Delta E_{\text{ZPE}}$  is the change of zero-point correction energy,  $\Delta S$  is the change of the entropy gradient, and  $T$  is the temperature.

$$\Delta G_U = -neU, \quad (5)$$

where  $e$  is the fundamental charge transfer,  $n$  is the proton–electron logarithm transferred, and  $U$  is the electrode applied potential relative to the RHE.

The overpotential ( $\eta$ ) of CO<sub>2</sub>RR is defined as follows:

$$\eta = U_{\text{equilibrium}} - U_{\text{limiting}}, \quad (6)$$

where  $U_{\text{equilibrium}}$  is the equilibrium potential of CO<sub>2</sub>RR. The limiting potential  $U_{\text{limiting}}$  is calculated as  $U_{\text{limiting}} = -\Delta G/e$ , where  $\Delta G_{\text{limiting}}$  represents the free energy of the potential-limiting step.

Carbon nanotubes (CNTs) are promising substitutes that have been widely applied in electrocatalysts for their high electrical conductivity, thermal stability, and abundant catalytic active sites (Grimme et al., 2010; Xiong et al., 2019; Bulmer et al., 2021; Cai et al., 2021). As an N-doped CNT (Figure 1A) may further increase

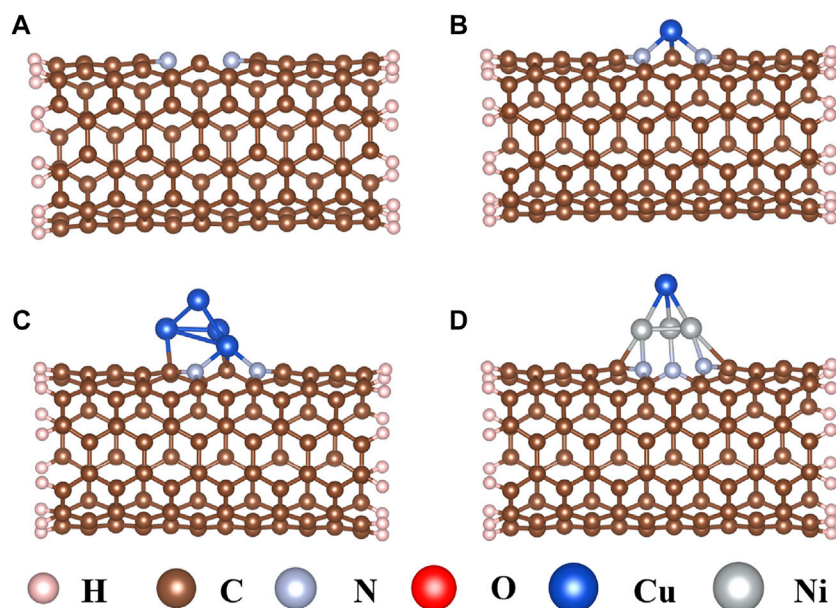


FIGURE 1

Optimized structures of (A) nitrogen-doped carbon nanotubes, (B) single Cu atom (Cu@CNTs), (C) Cu<sub>4</sub> cluster (Cu<sub>4</sub>@CNTs), and (D) CuNi<sub>3</sub> (CuNi<sub>3</sub>@CNTs) supported on the nitrogen-doped carbon nanotubes.

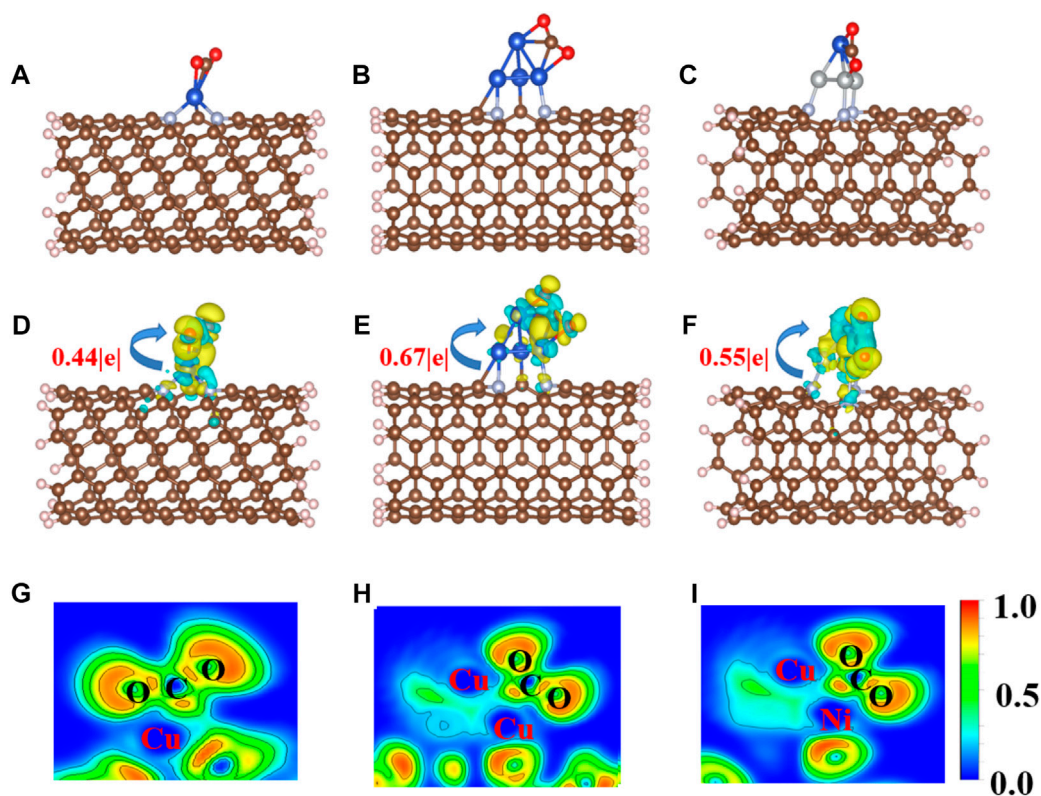


FIGURE 2

(A–C) Optimized adsorption configurations of CO<sub>2</sub> on Cu@CNTs, Cu<sub>4</sub>@CNTs, and CuNi<sub>3</sub>@CNTs. (D–F) Calculated charge density difference (CDD) and (G–I) the electronic local function diagram (ELF) of CO<sub>2</sub> adsorption. The charge depletion and accumulation are depicted in blue and yellow, respectively. The equivalent face value is 0.005 e/Å<sup>-3</sup>.

**TABLE 1** Geometric and electronic structure parameters of adsorbed \*CO<sub>2</sub> on the three Cu-based catalysts.

System	$E_{\text{ads}}$ (eV) <sup>*a</sup>	$\Delta\text{Angle}$ (degree) <sup>*b</sup>	$\Delta q$ ( e ) <sup>*c</sup>	ICOHP (eV) <sup>*d</sup>
Cu@CNTs	-0.50	146.74	0.44	-4.47
Cu <sub>4</sub> @CNTs	-0.19	140.77	0.67	-4.43
CuNi <sub>3</sub> @CNTs	-0.82	139.23	0.55	-3.82

\*a, adsorption energy of adsorbed CO<sub>2</sub>; \*b, bond angle of adsorbed CO<sub>2</sub>; \*c, number of electrons obtained by adsorbed \*CO<sub>2</sub>; \*d, values of the crystal integral Hamiltonian population (ICOHP) for the C and O atoms in the adsorbed \*CO<sub>2</sub> molecules.

interaction between CNT and the active center (Park et al., 2020; Nguyen and Shim, 2021), a single Cu atom, Cu<sub>4</sub> cluster, and CuNi<sub>3</sub> cluster were doped on the N-doped CNTs through the carbon vacancy defect to explore the effects on the CO<sub>2</sub>RR sizes and composition (Figures 1B–D). As shown in Figure 1B, the single Cu atom is connected to two N atoms and one C atom to form a pyramid-like structure with  $E_b$  values of -3.21 eV. The bond lengths of Cu–N and Cu–C are 2.11 Å and 1.80 Å, respectively. When the Cu<sub>4</sub> cluster is doped on the N-doped carbon nanotubes, the three Cu atoms at the bottom interact with two N atoms and two C atoms (Figure 1C), resulting in a strong interaction with  $E_b$  values of -4.87 eV. The Cu–N, Cu–C, and Cu–Cu bond lengths are 2.05 Å, 2.03 Å, and 2.42 Å, respectively. In addition, CuNi<sub>3</sub>@CNTs are used to study the compositional effect of Cu-based catalysts for CO<sub>2</sub>RR by replacing three Cu atoms in Cu<sub>4</sub>@CNTs with three Ni atoms connected to the adjacent N atoms and C atoms on the bottom of the tetrahedron, respectively (Figure 1D). The binding energy of CuNi<sub>3</sub>@CNTs is -5.12 eV. The large binding energies indicate that the three different Cu-based catalysts all possess high thermodynamic stability, ensuring their long-term use.

## 3 Results and discussion

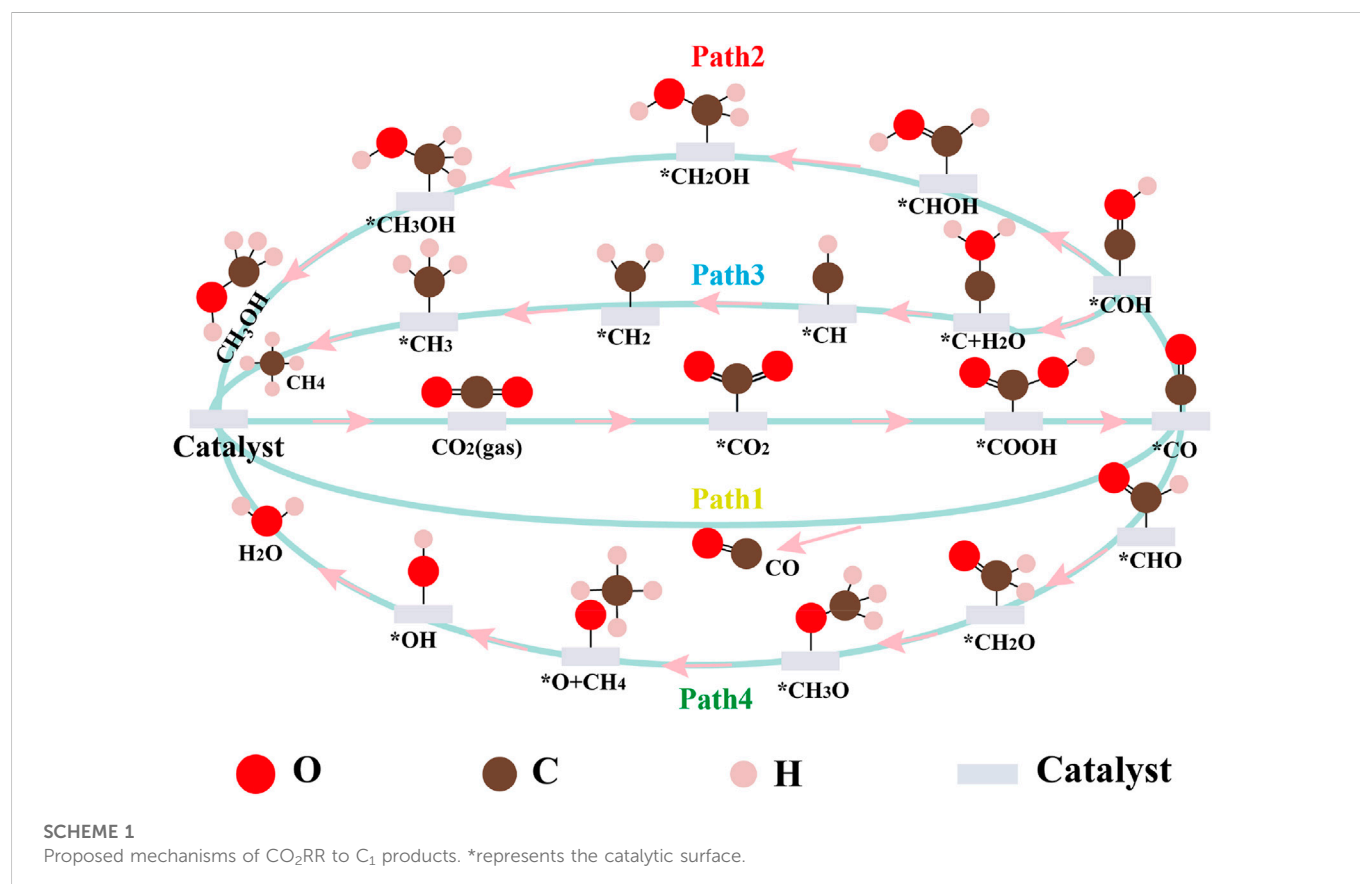
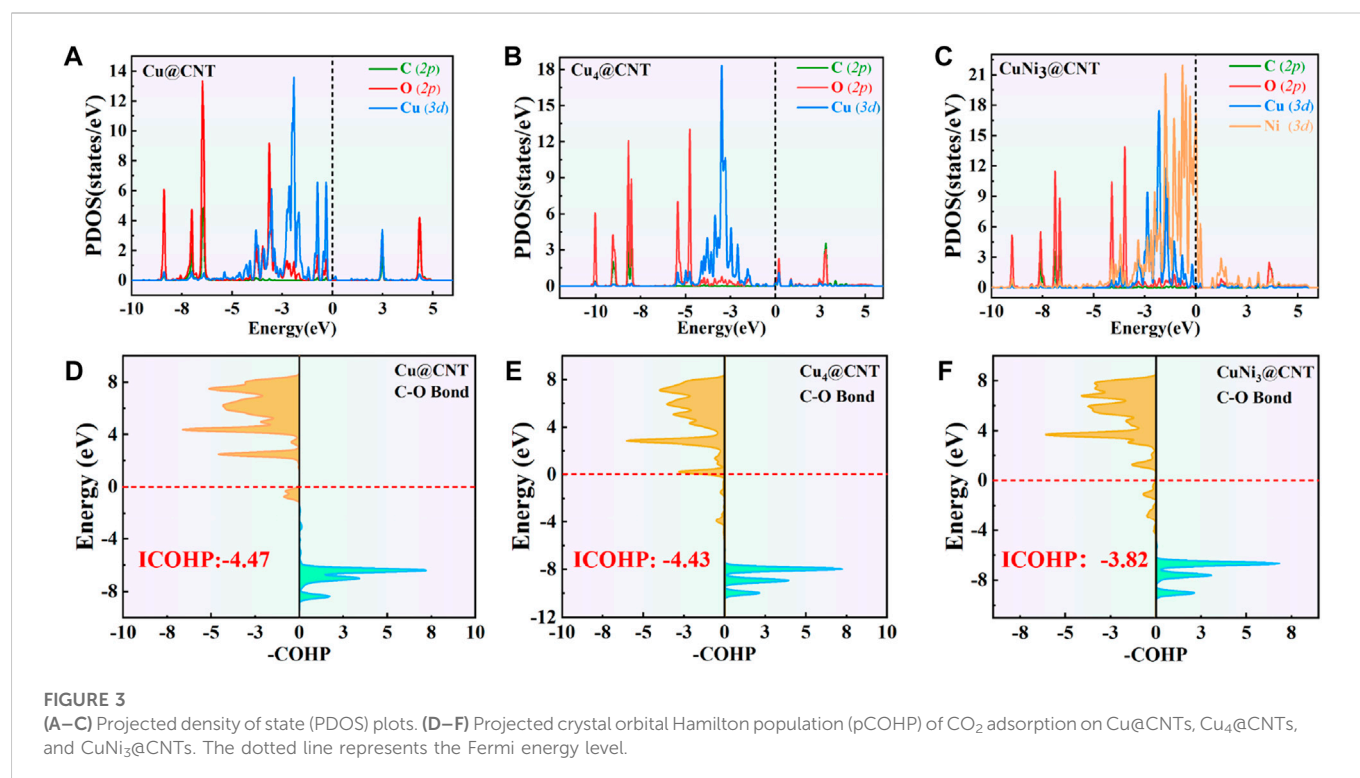
### 3.1 CO<sub>2</sub> activation on Cu@CNTs, Cu<sub>4</sub>@CNTs, and CuNi<sub>3</sub>@CNTs

CO<sub>2</sub> adsorption and activation are crucial steps for subsequent hydrogenation in CO<sub>2</sub>RR (Jiao et al., 2019). To investigate the behaviors of CO<sub>2</sub> adsorption, we explored the geometric and electronic structures of the adsorbed CO<sub>2</sub> molecules. As shown in Figure 2A, the CO<sub>2</sub> molecule is adsorbed on the single Cu atom site with an  $E_{\text{ads}}$  value of -0.50 eV. The C=O bond length in CO<sub>2</sub> is also slightly elongated from 1.18 to 1.25 Å. With increasing Cu active center size (from a single Cu atom to the Cu<sub>4</sub> cluster), the  $E_{\text{ads}}$  value of CO<sub>2</sub> decreases to -0.19 eV. The CO<sub>2</sub> prefers to adsorb on the edge site of the Cu<sub>4</sub> cluster (Figure 2B) compared to the top site, with an  $E_{\text{ads}}$  value of 0.15 eV. The adsorption site and configuration of CO<sub>2</sub> on the CuNi<sub>3</sub>@CNTs (Figure 2C) are the same as that on the Cu<sub>4</sub>@CNTs, although the  $E_{\text{ads}}$  value increases to -0.82 eV. The C=O bond length also increases to 1.26 Å. The top adsorption site of CuNi<sub>3</sub>@CNTs has an adsorption energy of 0.35 eV (Supplementary Figure S1). Thus, the top adsorption site was used for CO<sub>2</sub> molecule adsorption and activation on both the Cu<sub>4</sub>@CNTs and CuNi<sub>3</sub>@CNTs. The bond angles of O–C–O in the CO<sub>2</sub> molecule changed from 180.00° to 146.74°, 140.77°, and 139.23° on Cu@CNTs, Cu<sub>4</sub>@CNTs, and CuNi<sub>3</sub>@CNTs, respectively (Table 1). Thus, Cu@CNTs, Cu<sub>4</sub>@CNTs, and CuNi<sub>3</sub>@CNTs all significantly activate CO<sub>2</sub>, and the size and

composition effect greatly influence the degree of CO<sub>2</sub> activation, which may further affect the activity and selectivity of CO<sub>2</sub> hydrogenation.

To further investigate the activation mechanism of the CO<sub>2</sub> molecules, the Bader charge, charge density difference (CDD), electronic local function diagram (ELF), projected density of state (PDOS), and integrated crystal orbital Hamilton population (ICOHP) with CO<sub>2</sub> adsorption were investigated. As shown in Figures 2D–F, significant charge transfers occur between C=O double bonds and metal Cu and Ni atoms connected to CO<sub>2</sub>. In detail, the electron densities of the O atom, and between the C, O atoms and Cu, Ni atoms increase, while the electron density of the C=O double bond decreases significantly. In addition, the ELF map is used to further verify the bonding properties of C=O double bonds (Peterson et al., 2010; Reske et al., 2014; Wang et al., 2022). The results of the ELF calculation (Figures 2G–I) showed that the C=O double bond is weak, consistent with the results of the CDD analysis. The local electron densities of the Cu–C and Cu–O bonds range from 0.5 to 1.0 in the whole ELF map, which further verifies the metal coordination bond formation between Cu and Ni atoms and between the C and O atoms. The adsorbed \*CO<sub>2</sub> molecule gains 0.44|e|, 0.67|e|, and 0.55|e| from the Cu@CNTs, Cu<sub>4</sub>@CNTs, and CuNi<sub>3</sub>@CNTs, respectively, based on the Bader charge analysis, resulting in the bending of the bond angles of the adsorbed CO<sub>2</sub> molecules.

The PDOS of CO<sub>2</sub> adsorption are analyzed to further reveal interactions between Cu atoms and CO<sub>2</sub> (Figures 3A–C). The Cu-3d and Ni-3d orbitals play key roles in CO<sub>2</sub> adsorption and activation. The C-2p, O-2p, and Cu-3d orbitals have significant peak overlaps near the Fermi level, indicating strong interactions between C, O, and Cu atoms during CO<sub>2</sub> adsorption on Cu@CNTs and Cu<sub>4</sub>@CNTs (Figures 3A,B). With the introduction of the Ni atom, the Cu-3d and Ni-3d orbitals show hybridization, illustrating the strong interaction between the Cu and Ni atoms. Meanwhile, the broadly overlapped regions by C-2p, O-2p, Cu-3d, and Ni-3d hybrids also appear near-Fermi level, with strong peak intensities (Figure 3C). Based on the CDD and PDOS results, the mechanism of CO<sub>2</sub> activation can be summarized as follows: anti-bonding orbitals of CO<sub>2</sub> accept 3d-electrons from the Cu-3d and Ni-3d orbitals; meanwhile, the  $\pi$  electrons from the CO<sub>2</sub> bonding orbitals revert to empty Cu-3d and Ni-3d orbitals. The activation strength of the C=O double bond of the adsorbed CO<sub>2</sub> molecule is quantitatively studied by calculating the ICOHP values, in which lower values indicate stronger bond strength (Li et al., 2021; Song et al., 2021). As seen in Figures 3D–F, the C=O double bond anti-bonding states move down relative to the Fermi level after CO<sub>2</sub> adsorption. Therefore, the strength of the C=O double bond significantly decreases after CO<sub>2</sub> adsorption. The ICOHP values of the C=O double bond are -4.47, -4.43, and -3.82 eV on Cu@CNTs, Cu<sub>4</sub>@CNTs, and CuNi<sub>3</sub>@CNTs, respectively. The weaker the C=O double



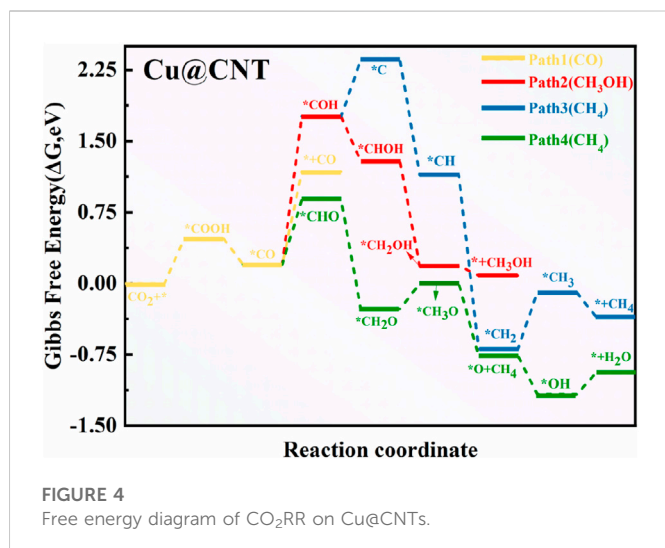


FIGURE 4  
Free energy diagram of CO<sub>2</sub>RR on Cu@CNTs.

bond, the more efficient the CO<sub>2</sub> activation on the catalyst surface. This result demonstrates the higher degree of CO<sub>2</sub> activation on the CuNi<sub>3</sub>@CNTs compared to that of the Cu@CNTs and Cu<sub>4</sub>@CNTs, consistent with the results of Bader charge, CDD, and adsorption energy calculations.

### 3.2 Mechanisms of CO<sub>2</sub>RR on Cu-based catalysts

CO<sub>2</sub>RR is a complex reaction involving multi-electron (two, six, or eight-electron) reaction pathways (Jiwanti and Einaga, 2019; Niu et al., 2021; Yang et al., 2022). The overall reaction equation can be expressed as follows:



Scheme 1 shows the different reaction paths for CO<sub>2</sub>RR to C1 products (CO, CH<sub>4</sub>, and CH<sub>3</sub>OH). According to the aforementioned description, the first step is CO<sub>2</sub> adsorption. Then, an electron from the catalyst surface attacks the adsorbed \*CO<sub>2</sub> molecules to form the radical CO<sub>2</sub><sup>-</sup>, resulting in the bending of the angle of the adsorbed \*CO<sub>2</sub>. Subsequently, the radical CO<sub>2</sub><sup>-</sup> intermediate combines with the H atom to form the key \*COOH intermediate. The \*COOH intermediate then is further hydrogenated to form \*CO and H<sub>2</sub>O. In Path 1, the adsorbed \*CO diffuses to the gas phase. In the other paths, the adsorbed \*CO species is further protonated to form \*COH or \*CHO *via* the formation of C-H or O-H bonds. Thus, CH<sub>4</sub> and CH<sub>3</sub>OH products can be obtained by further hydrogenation of the key intermediates \*COH or \*CHO. In Path 2, CH<sub>3</sub>OH is synthesized starting from the \*COH intermediate. The proton/electron pair (H<sup>+</sup>/e<sup>-</sup>) continuously attaches the C atom of \*COH to form the \*CHOH, \*CH<sub>2</sub>OH, and \*CH<sub>3</sub>OH intermediates. \*CH<sub>3</sub>OH then desorbs to form the CH<sub>3</sub>OH product. In contrast, CH<sub>4</sub> can be formed from \*CHO or \*COH *via* paths 3 and 4, respectively. In Path 3, the O atom of \*COH is hydrogenated to form H<sub>2</sub>O and \*C. In the next four hydrogenation steps, \*CH, \*CH<sub>2</sub>, \*CH<sub>3</sub>, and CH<sub>4</sub> are continuously generated. Moreover, the \*CHO intermediate can eventually be

protonated to produce CH<sub>4</sub> by the \*CH<sub>2</sub>O, \*CH<sub>3</sub>O, O\* + CH<sub>4</sub>, \*OH, and \*H<sub>2</sub>O species (Path 4). In addition, the C<sub>2</sub> products also can be synthesized on the Cu-based catalysts. However, when two CO<sub>2</sub> molecules are co-adsorbed on Cu@CNTs, Cu<sub>4</sub>@CNTs, and CuNi<sub>3</sub>@CNTs, only one CO<sub>2</sub> molecule can be adsorbed on the single-atom Cu, Cu<sub>4</sub> cluster, and CuNi<sub>3</sub> cluster; the other CO<sub>2</sub> molecule diffuses to the gas phase (Supplementary Figure S2). Therefore, this study explores only four paths for CO<sub>2</sub>RR to C1 products.

### 3.3 Reaction mechanism for CO<sub>2</sub>RR to CH<sub>4</sub> products on Cu@CNTs

To illustrate the catalytic activity and selectivity of CO<sub>2</sub>RR on Cu@CNTs, the free energy barrier diagram and corresponding intermediate configurations are shown in Figures 4, 5, respectively. Figure 4 shows that the adsorbed CO<sub>2</sub> molecule is hydrogenated to form stable \*COOH with a change of the free energy value (ΔG) of 0.47 eV. In the second hydrogenation step, \*COOH can react with the (H<sup>+</sup>/e<sup>-</sup>) pair to form \*CO and H<sub>2</sub>O, with an exothermic energy release of -0.27 eV. The adsorbed \*CO is further protonated to form \*CHO (ΔG = 0.61 eV) and \*COH (ΔG = 1.49 eV) intermediates, or may be directly desorbed with a ΔG value of 0.91 eV. Obviously, the formation of \*CHO is more favorable than that of \*CHO and \*CO desorption. When the \*COH species is formed, the C atom of \*COH accepts three H atoms to form \*CH<sub>3</sub>OH with downhill free energies of -0.47, -1.18, and -0.08 eV. \*COH is also directly dissociated into \*C species (ΔG = 0.60 eV), and \*CH<sub>4</sub> is formed by four hydrogenation steps of the \*C intermediate. The formation of \*CH and \*CH<sub>2</sub> is slightly thermodynamically favorable, with ΔG values of -1.22 and -1.83 eV, respectively. However, the formation of \*CH<sub>3</sub> has an endothermic energy of 0.78 eV. It is difficult to form the CH<sub>4</sub> molecule in Path 3 due to the high hydrogenation barrier of the formation of \*COH species for the whole reaction. In Path 4, \*CHO intermediate accepts an (H<sup>+</sup>/e<sup>-</sup>) pair to form \*CH<sub>2</sub>O with a ΔG value of -1.15 eV. Then, the hydrogenation of \*CH<sub>2</sub>O to \*CH<sub>3</sub>O is uphill by 0.26 eV. \*CH<sub>3</sub>O is further hydrogenated to form \*O and a CH<sub>4</sub> molecule with a ΔG value of -0.75 eV. The leaving \*O atom is continuously hydrogenated to form H<sub>2</sub>O. Thus, the conversion of CO<sub>2</sub> to CH<sub>4</sub> following Path 4 with an overpotential value of 0.37 V is easier than that of CO and CH<sub>3</sub>OH in all four paths, and the potential-determining step (PDS) is the \*CHO formation on the Cu@CNTs. Wang et al. prepared three Cu-based catalysts for CO<sub>2</sub>RR (Weng et al., 2018). Among them, the single-atom Cu phthalocyanine catalyst exhibited the highest activity to produce CH<sub>4</sub> with a Faradaic efficiency of 66% and a partial current density of 13 mA cm<sup>-2</sup> at a potential of -1.06 V versus RHE, findings that are consistent with the calculation results of CO<sub>2</sub>RR to CH<sub>4</sub> on the Cu-based single-atom catalysts in the present study.

### 3.4 Reaction mechanism for CO<sub>2</sub>RR to CO products on Cu<sub>4</sub>@CNTs

To explore the different size effects on CO<sub>2</sub>RR activity on Cu-based catalysts, the free energy profiles and optimized geometric structures for CO<sub>2</sub>RR on the Cu<sub>4</sub>@CNTs are shown in Figures 6, 7, respectively. The Cu<sub>4</sub> clusters embedded in the CNTs catalyst provided multiple active sites for the activation of CO<sub>2</sub> molecules compared to Cu@CNTs and further promoted hydrogenation. The adsorbed \*CO<sub>2</sub> accepts two (H<sup>+</sup>/e<sup>-</sup>) pairs to successively convert the key intermediates \*COOH and \*CO with an

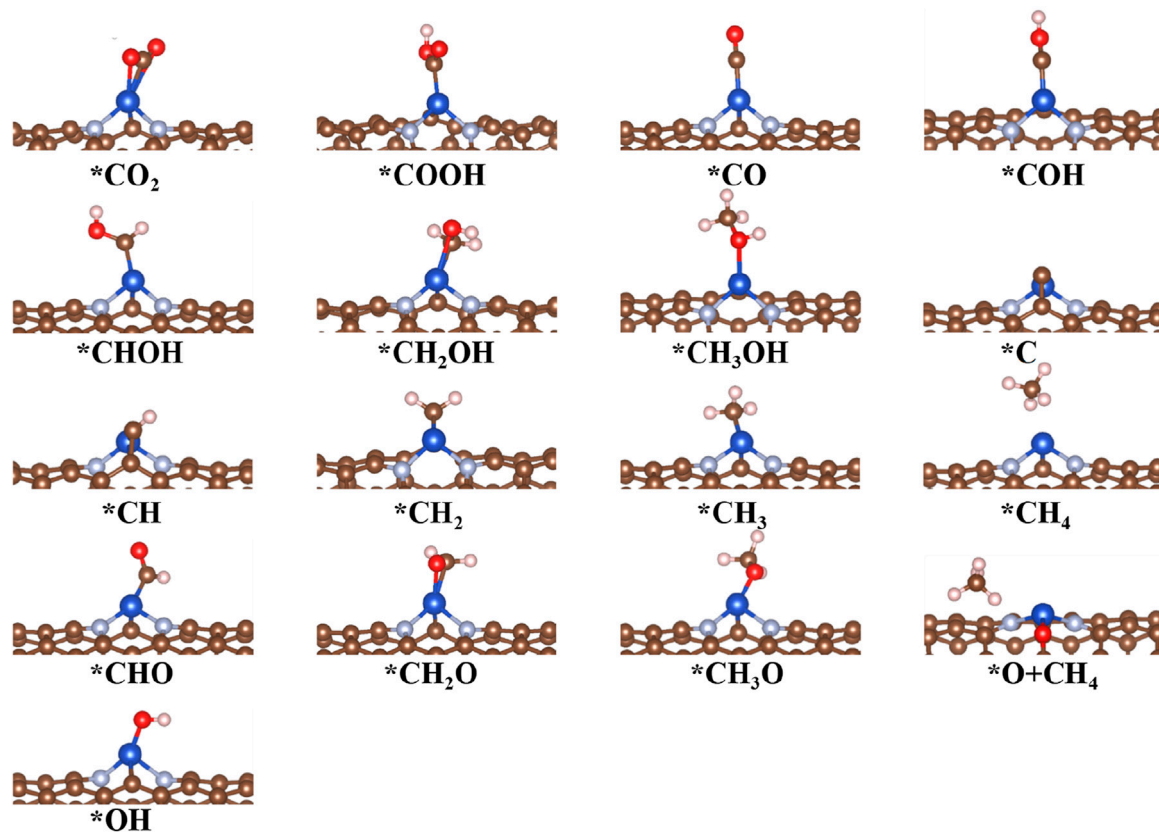


FIGURE 5 Optimized structures of intermediates for CO<sub>2</sub>RR on Cu@CNT surfaces.

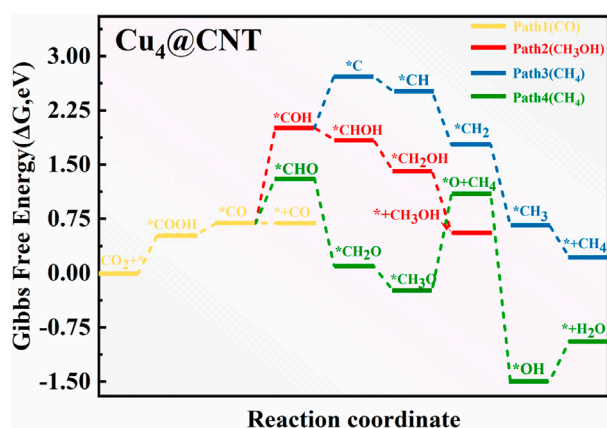


FIGURE 6 Free energy diagram of CO<sub>2</sub>RR on Cu<sub>4</sub>@CNTs.

entirely endothermic process of 0.54 eV and 0.16 eV, respectively. CO desorption is a thermodynamically favorable process with a low energy of  $-0.01$  eV compared to  $*\text{CO}$  hydrogenation to  $*\text{COH}$  ( $\Delta G = 1.32$  eV) and  $*\text{CHO}$  ( $\Delta G = 0.62$  eV). In the subsequent hydrogenation steps, the ( $\text{H}^+/\text{e}^-$ ) pair consecutively attacks the C atom of the  $*\text{CO}$  intermediates to form  $*\text{CHO}$ ,  $*\text{CH}_2\text{O}$ ,  $*\text{CH}_3\text{O}$ , and  $*\text{O}+\text{CH}_4$  species, with PDS, the process of  $*\text{O}+\text{CH}_4$  intermediate formation, with  $\Delta G$  values of 1.32 eV in Path 4.

After  $*\text{COH}$  formation,  $*\text{COH}$  hydrogen dissociates to form  $*\text{C}$  with an uphill energy of 0.72 eV. Then, the  $*\text{C}$  species is further hydrogenated to form  $*\text{CH}$ ,  $*\text{CH}_2$ ,  $*\text{CH}_3$ , and  $*\text{CH}_4$  (Path 3). The corresponding  $\Delta G$  values are  $-0.21$ ,  $-0.74$ ,  $-1.11$ , and  $-0.44$  eV, respectively. In Path 2,  $*\text{COH}$  is hydrogenated to form  $*\text{CHOH}$ ,  $*\text{CH}_2\text{OH}$ , and  $*\text{CH}_3\text{OH}$  species, with  $\Delta G$  values of  $-0.17$ ,  $-0.43$ , and  $-0.86$  eV. Comparison of the  $\Delta G$  values of PDS in all four paths shows that the reactions are more likely to follow Path 1 and CO is produced on the Cu<sub>4</sub>@CNTs with an extremely low overpotential value of 0.02 V. More importantly, the desorption energy of CO is greatly reduced with increasing Cu size, which is conducive to the production of CO and avoids poisoning the active sites on the catalyst surface. In addition, the reported atom-pair catalyst with stable Cu<sub>1</sub><sup>0</sup>-Cu<sub>1</sub><sup>x+</sup> pair structures also shows high selectivity and activity for CO<sub>2</sub>RR to CO (Li et al., 2020b). Therefore, our calculation results of CO<sub>2</sub>RR on cluster catalysts are consistent with experimental results reported previously. These results demonstrate that CO<sub>2</sub>RR reduction product changes from CH<sub>4</sub> to CO when the size of Cu-based catalysts changes from a single atom to a Cu<sub>4</sub> cluster. Therefore, designing multiple active sites to change the final reduction products may be a universal strategy for catalyst development.

### 3.5 Reaction mechanism for CO<sub>2</sub>RR to CH<sub>4</sub> products on CuNi<sub>3</sub>@CNTs

To explore the composition effect on the mechanism of CO<sub>2</sub>RR, the synthesis paths of CO<sub>2</sub> into CH<sub>4</sub>, CO, and CH<sub>3</sub>OH products

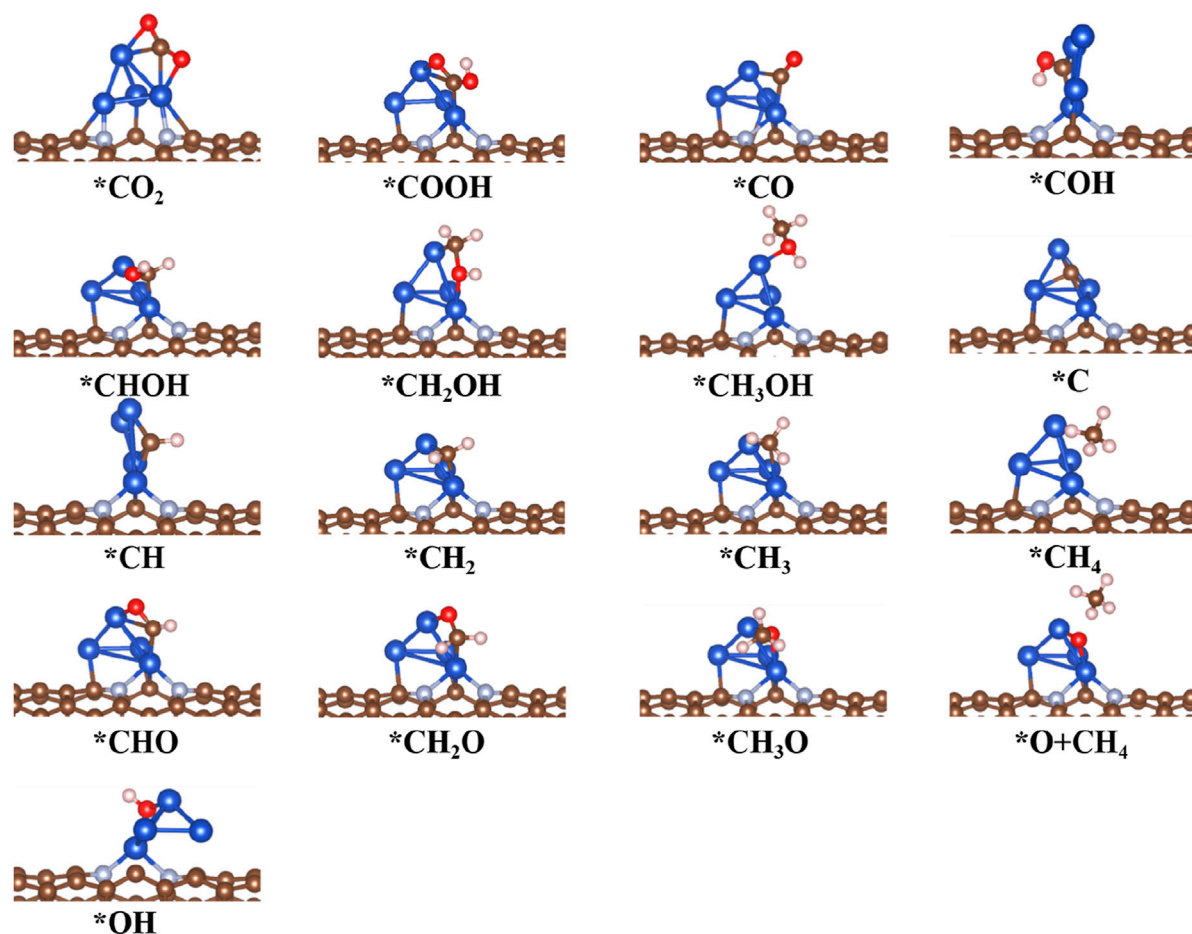


FIGURE 7  
Optimized structure of intermediates for CO<sub>2</sub>RR on Cu<sub>4</sub>@CNT surfaces.

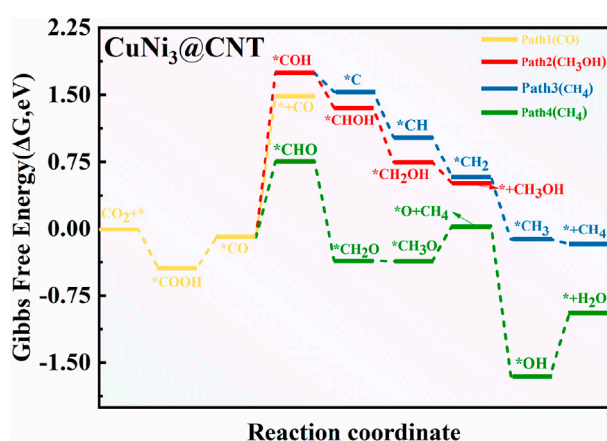


FIGURE 8  
Free energy diagram of CO<sub>2</sub>RR on CuNi<sub>3</sub>@CNTs.

were determined on CuNi<sub>3</sub>@CNTs. The free energy and geometric structure diagrams are shown in Figures 8, 9, respectively. The \*COOH intermediate is obtained in the first step of hydrogenation

of the adsorbed \*CO<sub>2</sub> molecule, with a downhill energy of  $-0.44$  eV on the CuNi<sub>3</sub>@CNTs catalyst, which differs from that on Cu@CNTs and Cu<sub>4</sub>@CNTs. According to the aforementioned charge transfer analysis, the adsorbed \*CO<sub>2</sub> molecule obtains more electrons from CuNi<sub>3</sub>@CNTs compared to Cu@CNTs and Cu<sub>4</sub>@CNTs, and the electrons of Ni-3d orbitals are partly transferred to the  $\pi$  anti-bonding orbitals of CO<sub>2</sub>. These strong electron transfers lead to the spontaneous formation of a \*COOH intermediate. The production of \*CO occurs through \*COOH hydrogenation to \*CO and H<sub>2</sub>O molecules. However, \*CO desorption requires a large desorption energy of 1.57 eV (Path 1). Thus, \*CO is further hydrogenated to \*COH ( $\Delta G = 1.83$  eV) or \*CHO ( $\Delta G = 0.84$  eV). In the subsequent hydrogenation steps, \*CHO is hydrogenated in two steps to form \*CH<sub>2</sub>O and \*CH<sub>3</sub>O in Path 4. Then, the (H<sup>+</sup>/e<sup>-</sup>) pair attacks the C atom in \*CH<sub>3</sub>O, resulting in CH<sub>4</sub> formation. After release of the CH<sub>4</sub> molecule, one \*O atom remains above the bridge site of the Cu-Ni atoms (Figure 9) and is subsequently further hydrogenated into H<sub>2</sub>O molecules and released. The reactions are more likely to follow Path 2 to form CH<sub>3</sub>OH than Path 3 to form CH<sub>4</sub> based on a comparison of the  $\Delta G$  values of producing possible species (\*CHOH, \*CH<sub>2</sub>OH; \*C, \*CH<sub>2</sub>, and \*CH<sub>3</sub>). As discussed previously, CO<sub>2</sub>RR is more likely to follow Path 4 to form CH<sub>4</sub> on CuNi<sub>3</sub>@CNTs, with an overpotential value of 0.60 V and \*COH

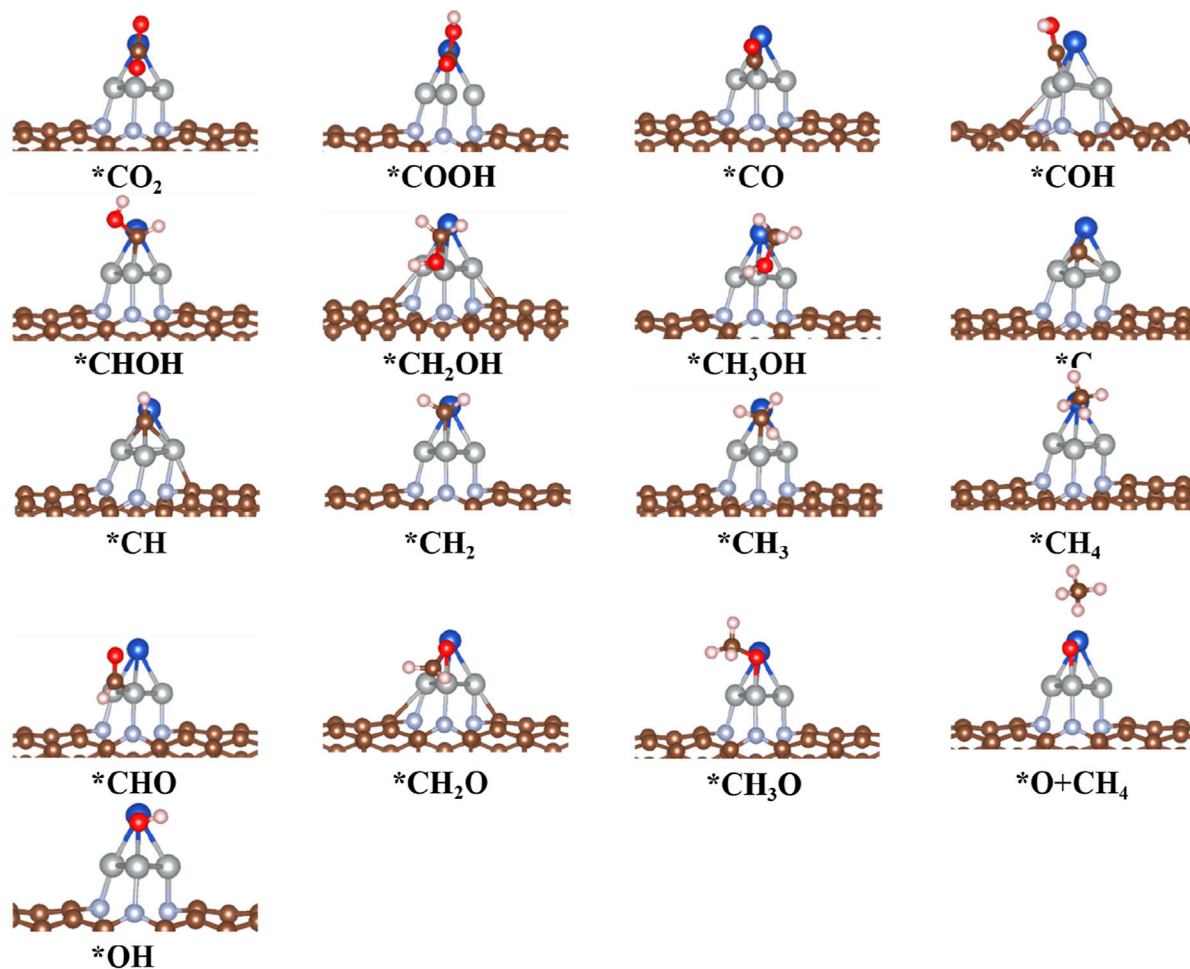


FIGURE 9  
Optimized structure of intermediates for CO<sub>2</sub>RR on the CuNi<sub>3</sub>@CNT surfaces.

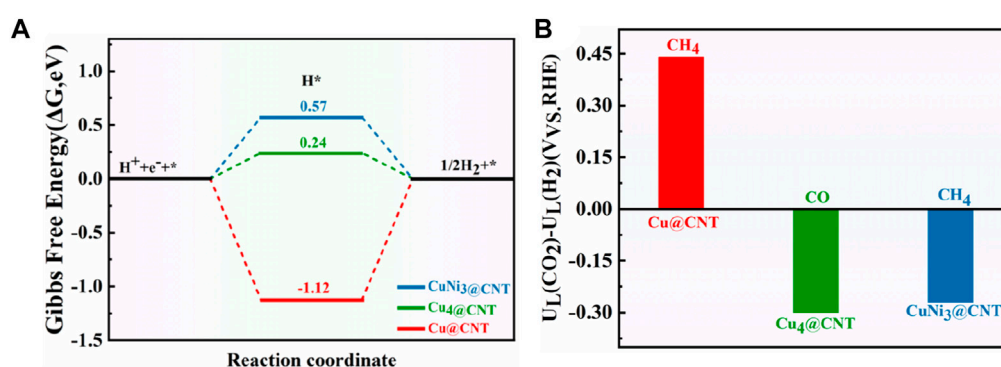


FIGURE 10  
(A) Free energy diagram of the HER on Cu@CNTs, Cu<sub>4</sub>@CNTs, and CuNi<sub>3</sub>@CNTs. (B) Differences in limiting potentials for CO<sub>2</sub>RR and HER on Cu@CNTs, Cu<sub>4</sub>@CNTs, and CuNi<sub>3</sub>@CNTs.

formation being the PDS. For the Cu–Ni alloy catalysts, the major products of CO<sub>2</sub>RR change from ethylene (C<sub>2</sub>H<sub>4</sub>) and C<sub>2</sub>H<sub>5</sub>OH to CH<sub>4</sub> with increasing Ni content (Park et al., 2021). These selectivity challenges are attributed to the increased adsorption energies of

\*CO on the Ni surface based on the results of pressure-dependent experiments and DFT calculations. We observed similar findings in our calculations. The  $E_{\text{ads}}$  values of \*CO on the CuNi<sub>3</sub>@CNTs are much higher than those on the Cu@CNTs and Cu<sub>4</sub>@CNTs. Thus,

the introduction of Ni atoms in the CuNi<sub>3</sub>@CNTs changes the selectivity of CO<sub>2</sub>RR to produce CH<sub>4</sub> compared to that on the Cu<sub>4</sub>@CNTs, which produce CO.

### 3.6 Competitive relationship of CO<sub>2</sub>RR vs. hydrogen evolution reaction (HER)

The hydrogen evolution reaction (HER) is usually considered a competitive reaction during CO<sub>2</sub>RR. Therefore, the selectivity and activity of CO<sub>2</sub>RR are tightly related to HER performance (Xue et al., 2020; Zhao and Liu, 2020). Figure 10A shows the free energies of HER for Cu@CNTs, Cu<sub>4</sub>@CNTs, and CuNi<sub>3</sub>@CNTs. HER occurs on three catalysts with  $\Delta G$  values of  $-1.12$ ,  $0.24$ , and  $0.57$  eV, respectively. The difference in limiting potentials for CO<sub>2</sub>RR and HER on Cu@CNTs, Cu<sub>4</sub>@CNTs, and CuNi<sub>3</sub>@CNTs were also calculated to further understand the selectivity of the catalyst for CH<sub>4</sub> or CO formation. The optimized configurations of \*H adsorption are shown in Supplementary Figure S3. The higher the  $U_L(\text{CO}_2) - U_L(\text{H}_2)$  difference, the higher is the selectivity for CO<sub>2</sub>RR over HER (Shen et al., 2021; Wei et al., 2021). As shown in Figure 10B, the selectivity toward CO<sub>2</sub>RR decreases in the order of Cu@CNTs (CH<sub>4</sub> product) > CuNi<sub>3</sub>@CNTs (CH<sub>4</sub> product) > Cu<sub>4</sub>@CNTs (CO product). The Cu@CNTs have only one adsorption site for the intermediates, while the CuNi<sub>3</sub>@CNTs and Cu<sub>4</sub>@CNTs have multiple adsorption sites (top, edge, and hollow sites). Thus, smaller-sized Cu@CNTs show the highest CH<sub>4</sub> selectivity among the three catalyst types. However, the large size of the bulk Ni (110) facet shows the highest selectivity for CH<sub>4</sub> compared to Ni@CNTs and Ni<sub>4</sub>@CNTs among the Ni-based catalysts (Cao, 2020b). In addition, the selectivity of CH<sub>4</sub> on the CuNi<sub>3</sub>@CNTs is higher than that for CO on the Cu<sub>4</sub>@CNTs. Therefore, the sizes and composition of Cu-based catalysts have a significant role in CO<sub>2</sub>RR selectivity.

## 4 Conclusion

In summary, the size and composition effect for the activity and selectivity of CO<sub>2</sub>RR were explored using DFT. Three types of Cu-based catalysts (Cu@CNTs, Cu<sub>4</sub>@CNTs, and CuNi<sub>3</sub>@CNTs) were designed to achieve highly efficient CO<sub>2</sub> reduction. The CuNi<sub>3</sub>@CNTs show the largest CO<sub>2</sub> adsorption energy ( $-0.82$  eV) due to CO<sub>2</sub> molecule adsorption on the edge site between the Ni and Cu atoms. This promotes higher charge transfer to CO<sub>2</sub> molecules and weakens the C=O double bond of CO<sub>2</sub>. With a size increase from single-atom Cu to the Cu<sub>4</sub> cluster, the CO<sub>2</sub>RR product changes from CH<sub>4</sub> to CO. More importantly, Cu<sub>4</sub>@CNTs show an extremely low overpotential of  $0.02$  V for CO formation, while Cu@CNTs exhibit the highest selectivity for CH<sub>4</sub> formation among the three catalysts. When the Ni atoms are introduced in the Cu<sub>4</sub> cluster, the CO<sub>2</sub>RR selectivity is improved compared to HER. The activity and selectivity of the Cu-based catalysts for the CO<sub>2</sub>RR depended strongly on the size and composition. Our results provide new

insight into understanding the size and alloy effect of CO<sub>2</sub>RR on Cu-based catalysts.

## Data availability statement

The original contributions presented in the study are included in the article/Supplementary Material; further inquiries can be directed to the corresponding authors.

## Author contributions

All authors listed have made a substantial, direct, and intellectual contribution to the work and approved it for publication.

## Funding

This work is financially supported by the National Natural Science Foundation of China (grant no. 22108093), the National Key Research and Development Program of China (grant no. 2018YFB1502900), the Natural Science Foundation of Zhejiang Province (grant nos. LY19B060006 and LQ20E030016), and the Innovation Jiaxing Elite Leadership Plan and Technology Development Project of Jiaxing University (70518040).

## Acknowledgments

The authors also acknowledge support from the G60 STI Valley Industry & Innovation Institute, Jiaxing University, and appreciate the help provided by J. H. Chen

## Conflict of interest

The authors declare that the research was conducted in the absence of any commercial or financial relationships that could be construed as a potential conflict of interest.

## Publisher's note

All claims expressed in this article are solely those of the authors and do not necessarily represent those of their affiliated organizations, or those of the publisher, the editors, and the reviewers. Any product that may be evaluated in this article, or claim that may be made by its manufacturer, is not guaranteed or endorsed by the publisher.

## Supplementary material

The Supplementary Material for this article can be found online at: <https://www.frontiersin.org/articles/10.3389/fchem.2023.1141453/full#supplementary-material>

## References

- Alvarez, A., Borges, M., Corral-Perez, J. J., Olcina, J. G., Urakawa, A., Cornu, D., et al. (2017). CO<sub>2</sub> activation over catalytic surfaces. *Chemphyschem* 18, 3135–3141. doi:10.1002/cphc.201700782
- Bai, X., Li, Q., Shi, L., Niu, X., Ling, C., and Wang, J. (2020). Hybrid Cu(0) and Cu(x) as atomic interfaces promote high-selectivity conversion of CO<sub>2</sub> to C<sub>2</sub>H<sub>5</sub>OH at low potential. *Small* 16, e1901981. doi:10.1002/smll.201901981
- Bloch, P. E. (1994). Projector augmented-wave method. *Phys. Rev. B* 50, 17953–17979. doi:10.1103/physrevb.50.17953
- Bulmer, J. S., Kaniyoor, A., and Elliott, J. A. (2021). A meta-analysis of conductive and strong carbon nanotube materials. *Adv. Mater.* 33, e2008432. doi:10.1002/adma.202008432
- Cai, Y., Fu, J., Zhou, Y., Chang, Y. C., Min, Q., Zhu, J. J., et al. (2021). Insights on forming N,O-coordinated Cu single-atom catalysts for electrochemical reduction CO<sub>2</sub> to methane. *Nat. Commun.* 12, 586. doi:10.1038/s41467-020-20769-x
- Cao, C., Zhao, C., Fang, Q., ZhongWang, J., Zhuang, G., Deng, S., et al. (2020b). Hydrogen peroxide electrochemical synthesis on hybrid double-atoms (Pd-Cu) doped N vacancy g-C<sub>3</sub>N<sub>4</sub>: A novel design strategy for electrocatalysts screening. *J. Mat. Chem. A* 8, 2672–2683. doi:10.1039/C9TA12468C
- Cao, C., Ma, D. D., Gu, J. F., Xie, X., Zeng, G., Li, X., et al. (2020a). Metal-organic layers leading to atomically thin bismuthene for efficient carbon dioxide electroreduction to liquid fuel. *Angew. Chem. Int. Ed. Engl.* 59, 15014–15020. doi:10.1002/anie.202005577
- Cao, Y., Zhao, J., Zhong, X., Yao, Z., Zhuang, G., Wang, J., et al. (2021). Building highly active hybrid double-atom sites in C<sub>2</sub>N for enhanced electrocatalytic hydrogen peroxide synthesis. *Green Energy Environ.* 6, 846–857. doi:10.1016/j.gee.2020.12.006
- Gong, Q., Ding, P., Xu, M., Zhou, W., Li, Y., Deng, J., et al. (2019). Structural defects on converted bismuth oxide nanotubes enable highly active electrocatalysis of carbon dioxide reduction. *Nat. Commun.* 10, 2807. doi:10.1038/s41467-019-10819-4
- Grimme, S., Antony, J., Ehrlich, S., and Krieg, H. (2010). A consistent and accurate *ab initio* parametrization of density functional dispersion correction (DFT-D) for the 94 elements H-Pu. *J. Chem. Phys.* 132, 154104. doi:10.1063/1.3382344
- Han, L., Song, S., Liu, M., Wu, Q., Luo, J., Xin, H. L., et al. (2020). Stable and efficient single-atom Zn catalyst for CO<sub>2</sub> reduction to CH<sub>4</sub>. *J. Am. Chem. Soc.* 142, 12563–12567. doi:10.1021/jacs.9b12111
- He, T., Zhang, L., Kour, G., and Du, A. (2020). Electrochemical reduction of carbon dioxide on precise number of Fe atoms anchored graphdiyne. *J. CO<sub>2</sub> Util.* 37, 272–277. doi:10.1016/j.jcou.2019.12.025
- Jiao, J. Q., Lin, R., Liu, S. J., Cheong, W. C., Li, Y. D., Chen, Z., et al. (2019). Copper atom-pair catalyst anchored on alloy nanowires for selective and efficient electrochemical reduction of CO<sub>2</sub>. *Nat. Chem.* 11, 222–228. doi:10.1038/s41557-018-0201-x
- Jiwanti, P. K., and Einaga, Y. (2019). Electrochemical reduction of CO<sub>2</sub> using palladium modified boron-doped diamond electrodes: Enhancing the production of CO. *Phys. Chem. Chem. Phys.* 21, 15297–15301. doi:10.1039/C9CP01409H
- Kresse, G., and Furthmüller, J. (1996). Efficiency of *ab-initio* total energy calculations for metals and semiconductors using a plane-wave basis set. *Comput. Mat. Sci.* 6, 15–50. doi:10.1016/0927-0256(96)00008-0
- Kresse, G., and Hafner, J. (1993). *Ab initio* molecular dynamics for liquid metals. *Phys. Rev. B* 47, 558–561. doi:10.1103/PhysRevB.47.558
- Kresse, G., and Joubert, D. (1999). From ultrasoft pseudopotentials to the projector augmented-wave method. *Phys. Rev. B* 59, 1758–1775. doi:10.1103/PhysRevB.59.1758
- Li, Q., Ouyang, Y., Lu, S., BaiZhang, X. Y., Shi, L., Ling, C., et al. (2020a). Perspective on the theoretical methods and modeling relating to electro-catalysis processes. *Chem. Commun.* 56, 9937–9949. doi:10.1039/D0CC02998J
- Li, Q., Wang, H., Luo, W., Sherrill, P. C., Chen, J., and Yang, J. (2020b). Heterogeneous single-atom catalysts for electrochemical CO<sub>2</sub> reduction reaction. *Adv. Mater.* 32, e2001848. doi:10.1002/adma.202001848
- Li, S., Nagarajan, A. V., Alfonso, D. R., Sun, M., Kauffman, D. R., Mpourmpakis, G., et al. (2021). Boosting CO<sub>2</sub> electrochemical reduction with atomically precise surface modification on gold nanoclusters. *Angew. Chem. Int. Ed. Engl.* 60, 6351–6356. doi:10.1002/anie.202016129
- Li, X., Bi, W., Chen, M., Sun, Y., Ju, H., Yan, W., et al. (2017). Exclusive Ni-N<sub>4</sub> sites realize near-unity CO selectivity for electrochemical CO<sub>2</sub> reduction. *J. Am. Chem. Soc.* 139, 14889–14892. doi:10.1021/jacs.7b09074
- Meng, Y., Xu, Z., Shen, Z., Xia, Q., Cao, Y., Wang, Y., et al. (2022). Understanding the water molecule effect in metal-free B-based electrocatalysts for electrochemical CO<sub>2</sub> reduction. *J. Mat. Chem. A* 10, 6508–6522. doi:10.1039/D1TA10127G
- Nadolska, M., Przesniak-Welenc, M., Lapinski, M., and Sadowska, K. (2021). Synthesis of phosphonated carbon nanotubes: New insight into carbon nanotubes functionalization. *Materials* 14, 2726. doi:10.3390/ma14112726
- Nguyen, A. T. N., and Shim, J. H. (2021). All carbon hybrid N-doped carbon dots/carbon nanotube structures as an efficient catalyst for the oxygen reduction reaction. *RSC Adv.* 11, 12520–12530. doi:10.1039/D1RA01197A
- Niu, H., Zhang, Z., Wang, X., Wan, X., Kuai, C., and Guo, Y. (2021). A feasible strategy for identifying single-atom catalysts toward electrochemical NO-to-NH<sub>3</sub> conversion. *Small* 17, e2102396. doi:10.1002/smll.202102396
- Park, B. J., Kim, J., and Park, H. S. (2020). Bifunctional electrocatalysts based on hierarchical graphene/iron hybrid architectures branched by N-doped CNT. *J. Alloys Compd.* 846, 156244. doi:10.1016/j.jallcom.2020.156244
- Park, J., Cho, M., Rhee, Y. M., and Jung, Y. (2021). Theoretical study on the degree of CO<sub>2</sub> activation in CO<sub>2</sub>-coordinated Ni(0) complexes. *ACS Omega* 6, 7646–7654. doi:10.1021/acsomega.0c06257
- Perdew, J. P., Burke, K., and Ernzerhof, M. (1996). Generalized gradient approximation made simple. *Phys. Rev. Lett.* 77, 3865–3868. doi:10.1103/PhysRevLett.77.3865
- Peterson, A. A., Pedersen, F. A., Studt, F., Rossmeisl, J., and Nørskov, J. K. (2010). How copper catalyzes the electroreduction of carbon dioxide into hydrocarbon fuels. *Energy Environ. Sci.* 3, 1311–1315. doi:10.1039/c0ee00071j
- Reske, R., Mistry, H., Behafarid, F., Cuenya, B. R., and Strasser, P. (2014). Particle size effects in the catalytic electroreduction of CO<sub>2</sub> on Cu nanoparticles. *J. Am. Chem. Soc.* 136, 6978–6986. doi:10.1021/ja500328k
- Shen, X., Liu, X., Wang, S., Chen, T., Zhang, W., Cao, L., et al. (2021). Synergistic modulation at atomically dispersed Fe/Au interface for selective CO<sub>2</sub> electroreduction. *Nano Lett.* 21, 686–692. doi:10.1021/acs.nanolett.0c04291
- Song, H., Tan, Y. C., Kim, B., Ringe, S., and Oh, J. (2021). Tunable product selectivity in electrochemical CO<sub>2</sub> reduction on well-mixed Ni–Cu alloys. *ACS Appl. Mat. Interfaces.* 13, 55272–55280. doi:10.1021/acscami.1c19224
- Wang, F., Meng, Y., Chen, X., Zhang, L., Li, G., Shen, Z., et al. (2022). Effect of nickel-based electrocatalyst size on electrochemical carbon dioxide reduction: A density functional theory study. *J. Colloid Interface Sci.* 615, 587–596. doi:10.1016/j.jcis.2022.02.032
- Wei, N., Tian, Y., Liao, Y., Komatsu, N., Kauppinen, E. I., Lyuleeva-Husemann, A., et al. (2021). Colors of single-wall carbon nanotubes. *Adv. Mater.* 33, e2006395. doi:10.1002/adma.202006395
- Weng, Z., Wu, Y. S., Wang, M. Y., Jiang, J. B., Wang, H. L., Huo, S., et al. (2018). Active sites of copper-complex catalytic materials for electrochemical carbon dioxide reduction. *Nat. Commun.* 9, 415. doi:10.1038/s41467-018-02819-7
- Xiong, W., Yang, J., Shuai, L., Qiu, M., Li, X., Hou, Y., et al. (2019). CuSn alloy nanoparticles on nitrogen-doped graphene for electrocatalytic CO<sub>2</sub> reduction. *ChemElectroChem* 6, 5951–5957. doi:10.1002/celec.201901381
- Xue, D., Xia, H., Yan, W., Zhang, J., and Mu, S. (2020). Defect engineering on carbon-based catalysts for electrocatalytic CO<sub>2</sub> reduction. *Nanomicro Lett.* 13, 5. doi:10.1007/s40820-020-00538-7
- Yang, T., Tian, N., Liu, X. H., and Zhang, X. (2022). CuNi alloy nanoparticles embedded in N-doped carbon framework for electrocatalytic reduction of CO<sub>2</sub> to CO. *J. Alloys Compd.* 904, 164042. doi:10.1016/j.jallcom.2022.164042
- Zhang, E., Wang, T. D., Zhang, J., Li, Y., Chen, W., Li, A., et al. (2019). Bismuth single atoms resulting from transformation of metal-organic frameworks and their use as electrocatalysts for CO<sub>2</sub> reduction. *J. Am. Chem. Soc.* 141, 16569–16573. doi:10.1021/jacs.9b08259
- Zhang, Y., Yang, R., Li, H., and Zeng, Z. (2022). Boosting electrocatalytic reduction of CO<sub>2</sub> to HCOOH on Ni single atom anchored WTe<sub>2</sub> monolayer. *Small* 18, e2203759. doi:10.1002/smll.202203759
- Zhao, X., and Liu, Y. (2020). Unveiling the active structure of single nickel atom catalysis: Critical roles of charge capacity and hydrogen bonding. *J. Am. Chem. Soc.* 142, 5773–5777. doi:10.1021/jacs.9b13872
- Zhong, M., Tran, K., Min, Y., Wang, C., Wang, Z., Ulissi, Z., et al. (2020). Accelerated discovery of CO<sub>2</sub> electrocatalysts using active machine learning. *Nature* 581, 178–183. doi:10.1038/s41586-020-2242-8
- Zhou, J., Wang, X., Ge, K., Yang, Z., Xia, L., Guo, C., et al. (2022). Core-shell structured nanocomposites formed by silicon coated carbon nanotubes with anti-oxidation and nanomagnetic wave absorption. *J. Colloid Interface Sci.* 607, 881–889. doi:10.1016/j.jcis.2021.09.022